

Variationally Consistent Framework for Finite-Strain Microelasticity

Tushar Jogi^{1*}

^{1*}Microstructure Physics and Alloy design, Max-Planck Institute for Sustainable Materials, Max-Planck Strasse 1, Düsseldorf, 40237, North-Rhine Westphalia, Germany.

Corresponding author(s). E-mail(s): t.jogi@mpi-susmat.de;

Abstract

Modeling microstructural evolution at large strains requires mechanical formulations that remain thermodynamically consistent while capturing significant lattice rotations and transformation-induced stresses. However, most existing finite-strain microelasticity and phase-field approaches apply macroscopic boundary conditions heuristically, preventing proper stress relaxation and violating the Hill–Mandel work equivalence required for homogenization. These limitations can misrepresent stress states and transformation pathways under finite strains. Here a variationally consistent finite-strain microelasticity framework is presented that couples microscopic and macroscopic mechanical equilibrium through a single energy functional. The resulting Euler–Lagrange conditions—periodic micro-equilibrium and macroscopic traction balance—are solved using a staggered FFT–Newton algorithm that combines a spectral fixed-point update for local fields with a Newton step for the homogenized deformation gradient. The formulation accommodates general hyperelastic constitutive laws and arbitrary transformation gradients.

Benchmarks demonstrate accurate recovery of small-strain Eshelby solutions and systematic nonlinear deviations at large dilatations. Applied to deformation twinning in magnesium, the framework reproduces lenticular morphology, stress redistribution, and faster lateral growth consistent with experiments.

This approach establishes a rigorous and scalable foundation for finite-strain phase-field simulations of coherent transformations under general stress or mixed boundary conditions.

Keywords: finite-strain, microelasticity, phase-field

1 Introduction

Coherent phase transformations, such as deformation twinning and martensitic transformations, are classic examples of displacive phase transformations in crystalline solids [1, 2]. These transformations involve a coordinated shear of the crystal lattice that leads to large local rotations and distortions, strongly influencing the morphology, variant selection, and mechanical behavior of materials. The evolution of such microstructures is governed by the interplay among lattice misfit, transformation strain compatibility, and long-range elastic interactions [3]. Since the pioneering work of [4–6], microelasticity theory has provided a rigorous thermodynamic framework to quantify these elastic interactions in coherent solids, forming the foundation of modern phase-field modeling of microstructural evolution.

Most conventional microelasticity and phase-field models, however, rely on the small-strain approximation, which assumes infinitesimal deformation and neglects geometric nonlinearity. This assumption becomes invalid when transformation strains are large or when significant lattice rotations develop, as is common in martensitic transformations and deformation twinning in hexagonal metals. Under such conditions, small-strain formulations can produce unrealistic stress distributions and fail to capture the correct twinning morphology and orientation relationships. Finite-strain formulations, based on multiplicative kinematics and hyperelastic constitutive laws, overcome these limitations by maintaining full rotational invariance and providing a more accurate description of systems with large distortions. These approaches have been used to simulate both martensitic and twinning phenomena under general loading conditions. Levitas et al. [7] proposed a Landau potential-based phase-field theory at large strains and employed the model to simulate multivariant displacive transformations using finite-element method (FEM). Hildebrand and Miehe [8] developed a phase-field formulation at finite strains to simulate the formation and dissipative evolution of two-variant martensitic twinned laminate microstructure using FEM. Phase-field finite-strain formulations have also been extended to integrate with crystal plasticity to model deformation twinning in hexagonal metals [9–12]. Other notable works on phase-field finite-strain formulations are [13–15]. Most previous studies employ finite-element or finite-difference schemes, which are orders of magnitude slower and often less efficient than spectral methods for micromechanical problems of comparable accuracy and resolution. [16, 17].

Despite these developments, most existing finite-strain phase-field formulations employ mechanically constrained boundary conditions, typically by prescribing a fixed macroscopic deformation (for example, [18]) or lack variational consistency under applied stress conditions. In such formulations, the representative volume element (RVE) is not allowed to relax macroscopically to accommodate the internal transformation strains that arise during spontaneous twin growth or martensitic transformation. Consequently, the Hill–Mandel principle of work equivalence is not satisfied, and the resulting driving forces for microstructural evolution become thermodynamically inconsistent. Furthermore, while fast Fourier transform–based spectral methods provide an efficient approach for solving mechanical equilibrium in periodic domains, they have rarely been coupled with an explicit macroscopic equilibrium condition within a finite-strain variational framework.

Table 1: Volume fraction of a spherical inclusion (radius 12.5) in different simulation domains.

Domain size	Volume fraction (%)
$256 \times 256 \times 256$	0.05
$128 \times 128 \times 128$	0.4
$64 \times 64 \times 64$	3

The objective of this work is to establish a variationally consistent framework for finite-strain microelasticity that explicitly couples microscopic and macroscopic equilibrium in a unified spectral setting. The formulation ensures energetic consistency and numerical robustness by deriving both microscopic and macroscopic balance conditions from a single thermodynamic potential. A staggered numerical algorithm combines an FFT-based solution for local mechanical equilibrium with a Newton-type update for the macroscopic deformation. The framework accommodates general hyperelastic constitutive models and transformation gradients that describe either deformation twinning or martensitic transformations. Benchmark studies and comparisons with classical inclusion problems demonstrate the accuracy, stability, and energetic consistency of the proposed approach.

2 Results

2.1 Eshelby inclusion as benchmark

A three-dimensional cubic domain is set up containing a spherical inclusion of radius 12.5, discretized on a grid with unit spacing. The domain size is $256 \times 256 \times 256$, while additional cases with $128 \times 128 \times 128$ and $64 \times 64 \times 64$ grids are used to vary the inclusion volume fraction. Both the inclusion and the matrix are assumed to be elastically isotropic, although the framework can readily incorporate anisotropic elastic constants. The eigen-dilatation levels considered are $\delta = 1\%$, 3% , 6% , 9% , 12% , 15% , 18% and 21% . For a given eigen-dilatation δ , the eigen deformation gradient is defined as

$$\mathbf{F}_i = \left(1 + \frac{\delta}{3}\right) \mathbf{I} = \mathbf{I} + \frac{1}{3} \begin{pmatrix} \delta & 0 & 0 \\ 0 & \delta & 0 \\ 0 & 0 & \delta \end{pmatrix}. \quad (1)$$

The isotropic elastic constants used are: shear modulus $\mu = 25$ GPa and Poisson’s ratio $\nu = 0.3$. The model is employed to investigate the influence of macroscopic boundary conditions—stress-controlled (coupled micro-macro) versus strain-controlled (micro-only)—on the mean stress response within the domain. The corresponding inclusion volume fractions with fixed radius for different simulation domain sizes are summarized in Table 1. The tolerance levels for micro-equilibrium and macro-equilibrium are set as $\varepsilon_{\text{tol}}^{\text{micro}} = 10^{-7}$ and $\varepsilon_{\text{tol}}^{\text{macro}} = 10^{-12}$.

The Eshelby inclusion problem serves as a classical benchmark for validating micromechanical solvers. In the small-strain limit, the stresses predicted by the finite-strain formulation should converge to the analytical Eshelby solution. Eshelby derived analytical expressions for the stress field inside an ellipsoidal inclusion undergoing a uniform dilatational eigenstrain and embedded in an infinite elastic medium, expressed in terms of elliptic integrals [19]. He subsequently extended the formalism to obtain the stress field in the surrounding matrix [20]. For a spherical inclusion with dilatation δ embedded in an isotropic elastic matrix, the analytical solution is [21]:

Inside the inclusion:

$$\sigma_{rr} = \sigma_{\theta\theta} = \sigma_{\phi\phi} = 2\mu \left[-\frac{2(1+\nu)}{3(1-\nu)} \frac{\delta}{3} \right], \quad (2)$$

In the matrix (with R_0 the inclusion radius and r the radial coordinate):

$$\sigma_{rr} = 2\mu \left[-\frac{2(1+\nu)}{3(1-\nu)} \left(\frac{R_0}{r} \right)^3 \frac{\delta}{3} \right], \quad (3)$$

$$\sigma_{\theta\theta} = \sigma_{\phi\phi} = 2\mu \left[\frac{(1+\nu)}{3(1-\nu)} \left(\frac{R_0}{r} \right)^3 \frac{\delta}{3} \right]. \quad (4)$$

Equilibrium simulations are conducted under two conditions: (i) micro-equilibrium (with fixed $\bar{\mathbf{F}} = \mathbf{I}$) and (ii) coupled micro–macro equilibrium where $\bar{\mathbf{F}}$ allowed to relax to accommodate applied load/traction. Figure 1 shows the number of iterations required to achieve convergence under micro-equilibrium, while Figure 2 illustrates the evolution of macro-residuals as a function of iteration number. For micro-equilibrium, convergence is attained within a maximum of six iterations in all cases. In contrast, for the coupled micro–macro equilibrium, up to 26 iterations may be required to reduce the residuals below 10^{-12} .

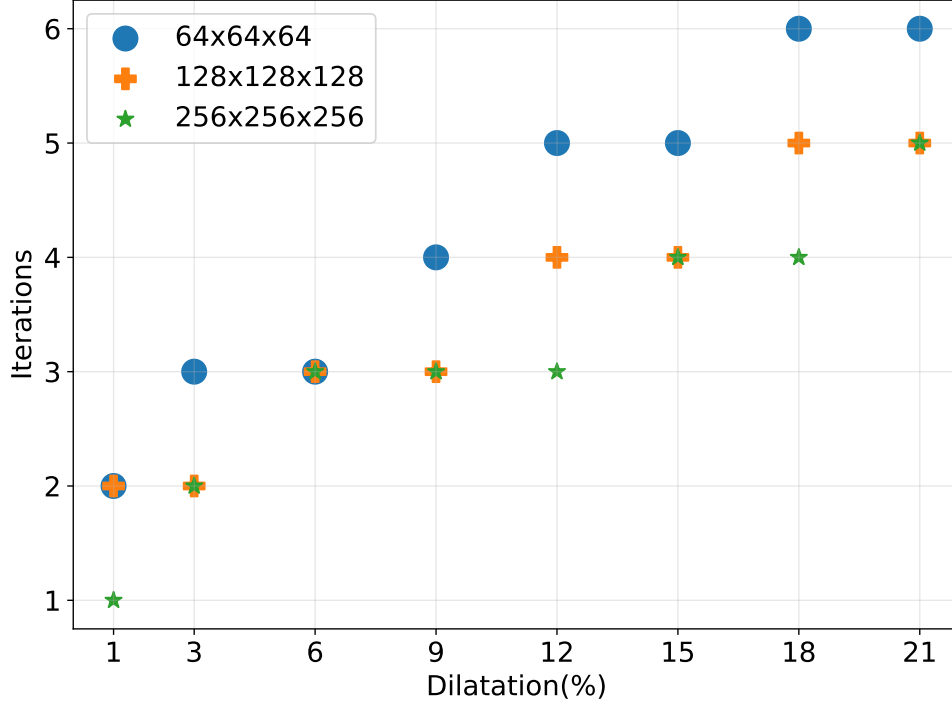


Fig. 1: Number of iterations for different levels of dilatation to achieve micro residual less than 10^{-6} .

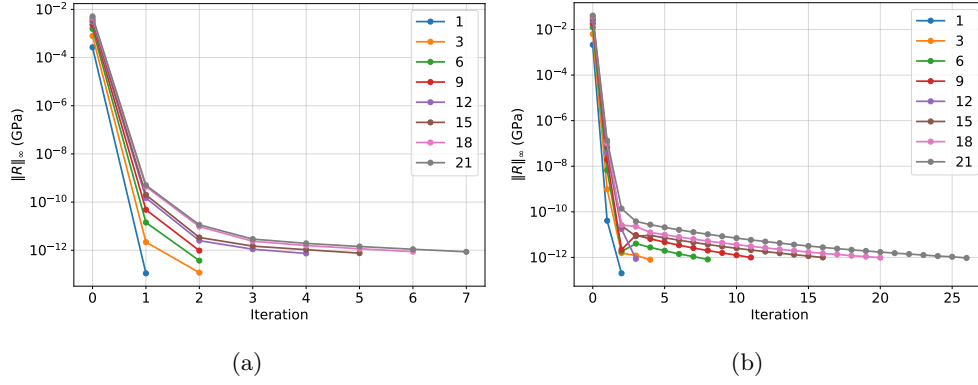


Fig. 2: Variation of macro residuals $\|R\|_{\infty}$ versus number of iteration at different levels of dilatations for (a) $256 \times 256 \times 256$ (b) $128 \times 128 \times 128$.

Figure 3 shows the predicted stress profiles across the inclusion center for various dilatation levels ($\delta = 1\%, 6\%, 12\%, 21\%$).

For $\delta = 1\%$, both numerical predictions closely reproduce the analytical Eshelby stress profile (see Fig. 3a). With increasing dilatation, the predicted stresses progressively deviate from the Eshelby solution, reflecting the nonlinear response captured by the finite-strain formulation but absent in Eshelby's linear-elastic theory. Figure 5(a) further compares the stress at the inclusion center with the analytical Eshelby stress and shows the corresponding relative error. The stress field agrees well at small dilatation levels (relative error less than 5%) but deviates progressively as dilatation increases. Overall, these results confirm that the predicted stress fields are consistent with Eshelby's inclusion theory in the small-strain limit and naturally extend beyond it under finite-strain conditions.

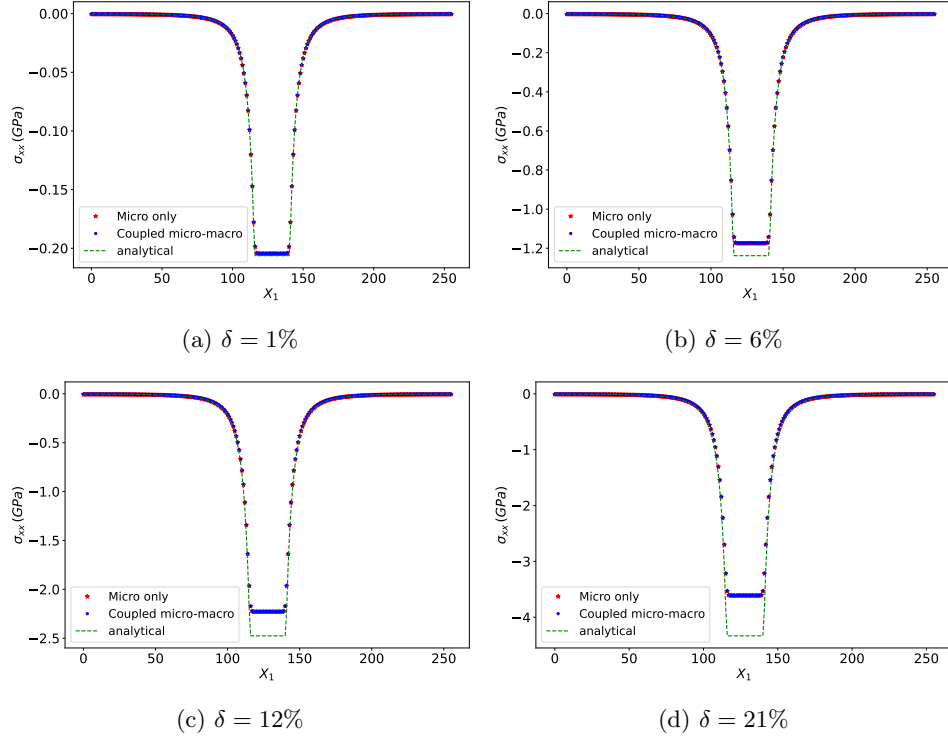


Fig. 3: Stress profile along X axis across the center of the inclusion and its comparison of predicted stress profile with analytical solution. The domain size is $256 \times 256 \times 256$

Figs. 4a and 4b show stress profiles across spherical inclusion embedded in domain size $128 \times 128 \times 128$ and $64 \times 64 \times 64$, respectively, for dilatational strain 12%. With

increase in volume fraction of inclusion, the predicted stresses deviate from analytical solution. However, under micro-equilibrium, the system exhibit a non-zero mean stresses, while coupled micro-macro equilibrium ensures zero mean stresses. Fig. 4c illustrates the variation of mean first Piola-Kirchhoff stress ($\bar{\mathbf{P}}$) for different levels of dilatational strain and inclusion volume fraction. The mean first Piola-Kirchhoff stress increases systematically with both dilatational strain and inclusion volume fraction. Under micro-equilibrium, the dilatational strain is internally balanced and stored as elastic energy, leading to residual mean stresses. On the other hand, under coupled micro-macro equilibrium, the same transformation strain manifests as a macroscopic deformation, allowing the system to relieve internal stresses while preserving global force balance.

Under fully clamped boundary conditions, the residual mean stresses play a consequential role in governing the evolution of coherent transformations such as twin growth or martensitic transformations. Since the global deformation is constrained, the transformation-induced eigenstrain may not relax through macroscopic shape change and could instead be retained as elastic energy within the system. The stored elastic energy can alter the effective thermodynamic driving force, potentially suppressing further phase growth or modifying the preferred transformation pathway. As the volume fraction of the transformed phase increases, the constraint imposed by the surrounding matrix is likely to intensify, leading to a proportional rise in the mean stress and, consequently, in the elastic energy penalty. In systems undergoing martensitic or twinning transformations, the presence of non-zero mean stress might promote the formation of self-accommodating variant pairs or complex twinned microstructures that minimize the macroscopic strain while preserving coherency. The transformation could therefore proceed through elastically compatible configurations rather than stress-free ones, which may lead to the development of internal back-stresses and possible transformation arrest once local strain accommodation is saturated. In contrast, under mixed or traction-free boundary conditions, partial relaxation of the transformation strain is possible through external deformation, interface migration, or plastic accommodation in the surrounding matrix. Under such conditions, the mean stress may reduce substantially or even vanish at macro-equilibrium, allowing the transformation to proceed more freely.

In reality, however, materials rarely experience perfectly clamped boundary conditions. Most systems evolve under mixed or traction-free boundary conditions, where partial relaxation of the transformation strain is possible through external deformation, interface migration, or plastic accommodation in the surrounding matrix. Under such conditions, the mean stress may reduce substantially or even vanish at macro-equilibrium, allowing the transformation to proceed more freely.

In the next section, I illustrate the effect of macroscopic conditions (fully clamped and uniaxial stress loading) on the evolution of deformation twinning.

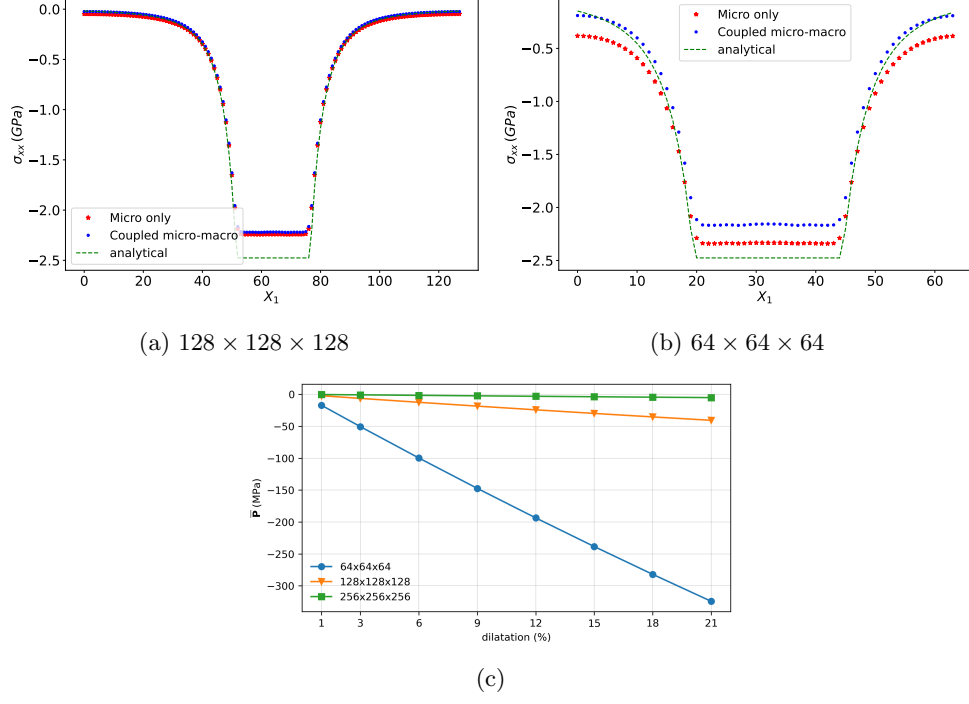


Fig. 4: Predicted stress profiles across a spherical inclusion for domain sizes (a) $128 \times 128 \times 128$ and (b) $64 \times 64 \times 64$ with a dilatational eigenstrain of $\delta = 12\%$. (c) Mean stress \bar{P} as a function of dilatational strain δ for varying inclusion volume fractions.

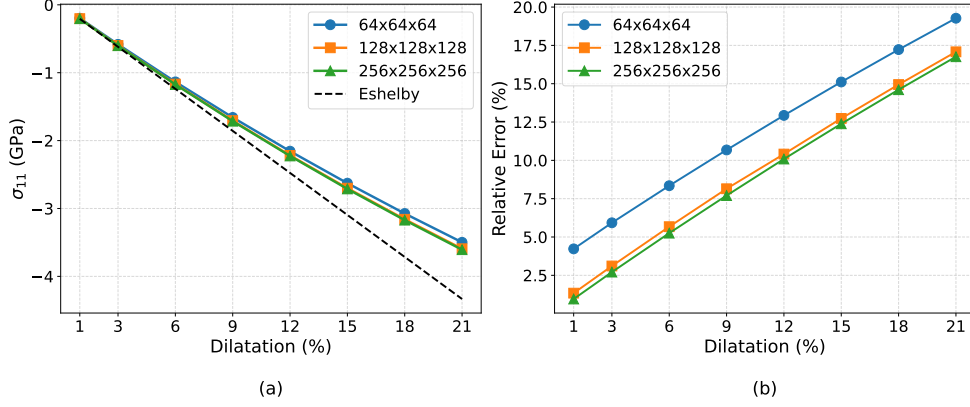


Fig. 5: (a) Variation of stress σ_{11} inside the inclusion as a function of dilatation as compared to analytical solution for different volume fractions of inclusion. (b) Relative error in stress with respect to analytical solution at various levels of dilatations for different volume fractions of inclusion.

2.2 Application of Variational Framework: morphological evolution of deformation twin

Deformation twinning is fundamentally mediated by the coordinated motion of twinning dislocations that glide on specific crystallographic planes and collectively reorient a region of the crystal lattice to produce a mirror-symmetric domain [22, 23]. From a mesoscale perspective, the morphology and evolution of the deformation twin are primarily an outcome of competition between long-range elastic interactions and interfacial energies. As long as the elastic strain fields associated with the twinning shear are preserved before significant recovery and the relaxation of coherency stresses, the 3D twin shape tends to minimize the total internal energy dominated by these contributions. This interpretation is further supported by recent high-resolution digital image correlation (DIC) studies in magnesium, which reveal that deformation twin can nucleate in regions both with and without prior slip, underscoring the influence of local stress states on twin formation [24]. Motivated by these insights, the present work employs a 3D phase-field model incorporating only elastic and interfacial energies to isolate their intrinsic role in controlling twin evolution.

In this work, deformation twinning is employed as a prototype phenomenon to demonstrate the capability of the present finite-strain framework for coupled evolution of microstructure and micromechanical fields. Although, theoretical foundations of deformation twinning are well established, most simulation studies are performed in two-dimensions [25–28] and three-dimensional work is limited [18]. Microscopic techniques show that the morphology of twin is always lenticular in bright side view (along $\lambda = K_1 \times \eta_1$) compared to irregular shape in twinning plane normal view (along K_1) [29, 30]. Moreover, it is observed that the twins grow faster along the lateral direction (λ) than along shear direction η_1 during initial stages of twin growth. Recently,

Zhao et al. developed phase-field finite-strain microelasticity theory and applied it to the morphological evolution of deformation twin in magnesium [18]. Their work shows that twin tip can be flattened under finite-strain framework, however, after introducing anisotropy in interface mobility leads to sharper twin tips.

Using the phase-field model, I simulate deformation twinning with single twin variant in a hexagonal matrix. The simulation domain is oriented such that laboratory coordinate axes $(\hat{x}, \hat{y}, \hat{z})$ coincide with (λ, η_1, K_1) , where $\eta_1 = \langle \bar{1}011 \rangle$, $K_1 = \langle 10\bar{1}2 \rangle$ and $\lambda = \eta_1 \times K_1$. Fig. 6 represents the initial configuration, where a small twinned region characterized by shear direction $\eta_1 = \langle \bar{1}011 \rangle$ and twin plane $K_1 = \{10\bar{1}2\}$. Initial twinned region is assumed to be a ellipsoidal disc with its plane oriented along K_1 and twin thickness of $t_{\text{twin}} = 1.875 \text{ nm}$ and length of 3.75 nm . The simulation parameters are listed in Table 2. Assuming experimentally measured twin boundary energy $E_{\text{twin}} = 120 \text{ mJ m}^{-2}$ [31] and twin boundary thickness $2\xi = 1 \text{ nm}$, the barrier potential A_1 and gradient energy coefficient κ is obtained as [32]

$$A_1 = \frac{6\alpha E_{\text{twin}}}{(2\xi)} \approx 2 \text{ J m}^{-3}, \quad \kappa = \frac{3E_{\text{twin}}(2\xi)}{2\alpha} = 6.14 \times 10^{-11} \text{ J m}^{-1}, \quad \alpha = 2.93$$

Lets assume the energy scale to be $\mathcal{E} = 1 \times 10^9 \text{ J m}^{-3}$, and considering minimum of four grids in the interface, the characteristic length comes out to be $\mathcal{L} = (2\xi)/4 = 0.25 \text{ nm}$. The dimensionless gradient energy coefficient is $\kappa^* = \kappa/(A_1 \mathcal{L}^2)$. All other quantities in dimensionless are given in the Table 2. The elastic constants for pure Magnesium are taken as $C_{11} = 59.4 \text{ GPa}$, $C_{12} = 25.6 \text{ GPa}$, $C_{13} = 43.7 \text{ GPa}$, $C_{33} = 61.7 \text{ GPa}$, $C_{44} = 16.4 \text{ GPa}$ [33]. With lattice parameters of Magnesium ($c = 0.521 \text{ nm}$ and $a = 0.3209 \text{ nm}$), the shear magnitude is obtained as [34]

$$\gamma = \frac{c}{\sqrt{3}a} - \frac{\sqrt{3}a}{c}.$$

With $\hat{y} \parallel \eta_1$ and $\hat{z} \parallel K_1$, the twinning shear acts along $\mathbf{s} = \hat{y}$ on the plane normal $\mathbf{n} = \hat{z}$. Hence, the resolved shear is $\tau_{\text{res}} = \boldsymbol{\sigma} : \mathbf{m}$ with $\mathbf{m} = \frac{1}{2}(\mathbf{s} \otimes \mathbf{n} + \mathbf{n} \otimes \mathbf{s})$. Creating a twin introduces two twin boundaries of energy $2E_{\text{twin}}$ per unit area, while the applied loading does mechanical work $\gamma \tau_{\text{res}} t_{\text{twin}}$ per unit area. Neglecting elastic mismatch terms, a simple and very useful growth criterion is

$$\gamma \tau_{\text{res}} t_{\text{twin}} \gtrsim 2E_{\text{twin}} \implies \tau_c = \frac{2E_{\text{twin}}}{\gamma t_{\text{twin}}}$$

Once the resolved shear stress exceeds τ_c , the twin is energetically favored to grow. The critical deformation gradient for twin to grow:

$$\bar{F}_c = \frac{\tau_c}{C_{44}}$$

With the chosen parameters in this work, the critical shear stress $\tau_c = 1 \text{ GPa}$ and critical deformation gradient is $\bar{F}_c = 0.06$. The loads used here ($\sigma_{23} = 2 \text{ GPa}$ or $\bar{F}_{23} = 0.1$) exceed these thresholds and therefore promote twin growth. Zhao et al. [18] suggested

Parameter	Dimensionless form	Value
Grid size (dx^*, dy^*, dz^*)	$dx^* = dx/\mathcal{L}$	1.0, 1.0, 1.0
Simulation domain (N_x, N_y, N_z)	—	128, 128, 128
Barrier potential (A_1^*)	$A_1^* = A_1/\mathcal{E}$	2.0
Gradient energy coefficient (κ_s^*)	$\kappa_s^* = \kappa_s/(A_1\mathcal{L}^2)$	0.5
Isotropic interface mobility (M_0^*)	—	1.0
Mobility coefficients (a_x, a_y, a_z)	—	1.5, 1.5, -0.95
Magnitude of twin shear (γ)	—	0.129
Elastic constants ($C_{11}^*, C_{12}^*, C_{13}^*, C_{33}^*, C_{44}^*$)	$C_{ij}^* = C_{ij}/\mathcal{E}$	59.7, 26.2, 21.7, 61.7, 16.4
Applied stress (σ_{ij}^*)	$\sigma_{ij}^* = \sigma_{ij}/\mathcal{E}$	[0, 0, 0.0, 0, 1.75, 0]
Applied deformation gradient ($\bar{\mathbf{F}}_{23}$)	—	0.11
micro iteration tolerance ($\epsilon_{\text{tol}}^{\text{micro}}$)	—	10^{-5}
macro iteration tolerance ($\epsilon_{\text{tol}}^{\text{macro}}$)	—	10^{-5}

Table 2: Simulation parameters

that experimentally observed sharp twin tips likely forms due to the anisotropy in interface mobility. Hence, I have introduced anisotropy by choosing $a_x = a_y = 1.5$ and $a_z = -0.95$, which ensures that interfaces normal to K_1 are fifty times slower than interfaces along K_1 .

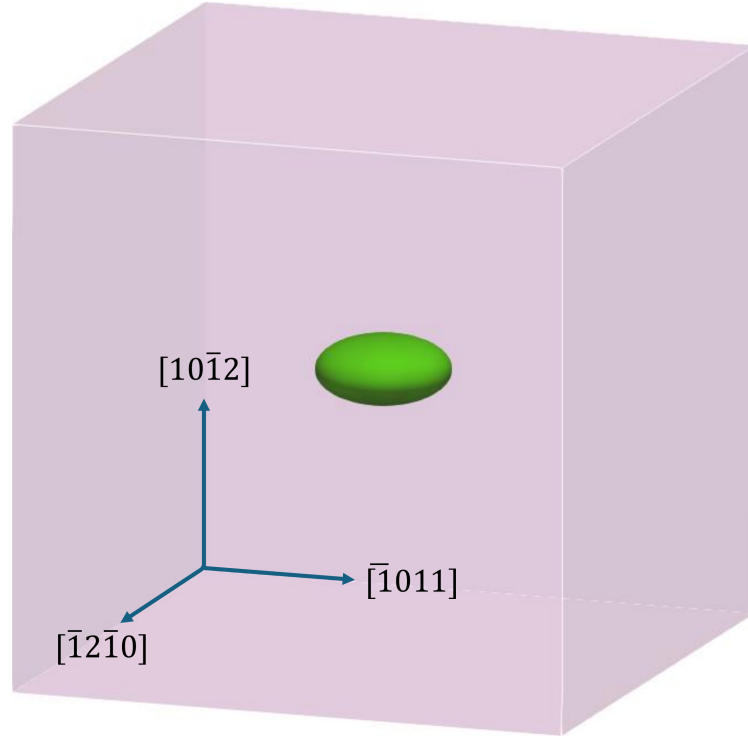
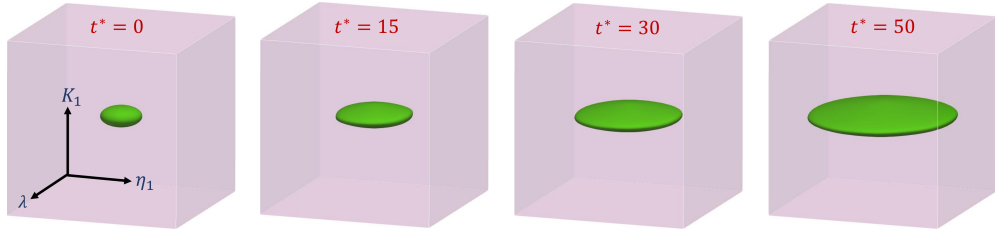
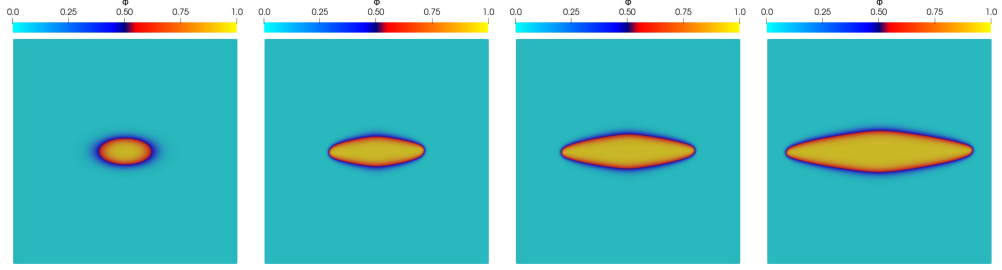


Fig. 6: Initial configuration comprising ellipsoidal twin nucleus present at the center of the simulation box. The laboratory axes $(\hat{x}, \hat{y}, \hat{z})$ are oriented along (λ, η_1, K_1) .

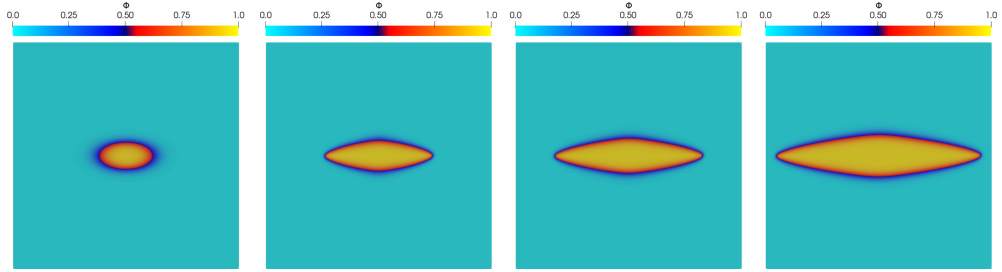
Figure 7 illustrates the evolution of the twin variant under applied deformation level. The twin morphology, viewed along λ and η_1 directions, confirms the lenticular morphology of twins. Crucially, the twin grows faster along λ direction as compared to forward propagation along η_1 (see Figure 8). This observation confirms the experimental results [29, 30], who reported faster twin propagation along the lateral direction (λ).



(a) 3D



(b) λ view



(c) η_1 view

Fig. 7: Evolution of twin morphology under deformation-controlled conditions

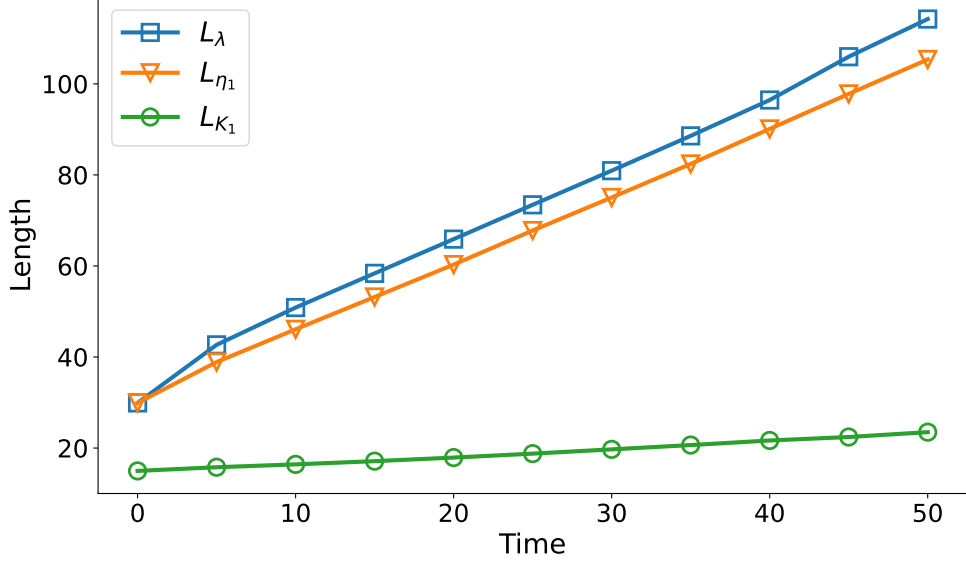


Fig. 8: Temporal evolution of twin lengths (dimensionless) along η_1 , K_1 and λ directions. Plot shows that twin grow faster along lateral direction (λ)

3 Method

Let $\Omega \subset \mathbb{R}^3$ denote a periodic reference domain (RVE) of volume V_0 , occupied by the hyperelastic body \mathcal{B}_0 with boundary ∂V_0 in the undeformed frame of reference. The deformation map $\chi : \Omega \rightarrow \mathbb{R}^3$ induces the deformation gradient

$$\mathbf{F}(\mathbf{X}) = \chi(\mathbf{X}) \otimes \nabla_{\mathbf{X}}, \quad \mathbf{X} \in \Omega. \quad (5)$$

Stress-free lattice distortions associated with coherent phase transformations are modeled by the multiplicative split

$$\mathbf{F} = \mathbf{F}_e \mathbf{F}_i, \quad \mathbf{F}_e := \mathbf{F} \mathbf{F}_i^{-1}. \quad (6)$$

Unless stated otherwise, $\mathbf{F}_i(\mathbf{X})$ is prescribed and we focus on mechanical equilibrium at finite strain.

The reference body is partitioned as $\Omega_0 = \mathcal{D}_M^0 \cup \mathcal{D}_I^0$ (matrix M and inclusion I). The transformation (eigen) gradient \mathbf{F}_i maps Ω_0 to an intermediate stress-free configuration Ω^* , producing

$$\mathcal{D}_M^* = \mathbf{F}_i(\mathcal{D}_M^0), \quad \mathcal{D}_I^* = \mathbf{F}_i(\mathcal{D}_I^0). \quad (7)$$

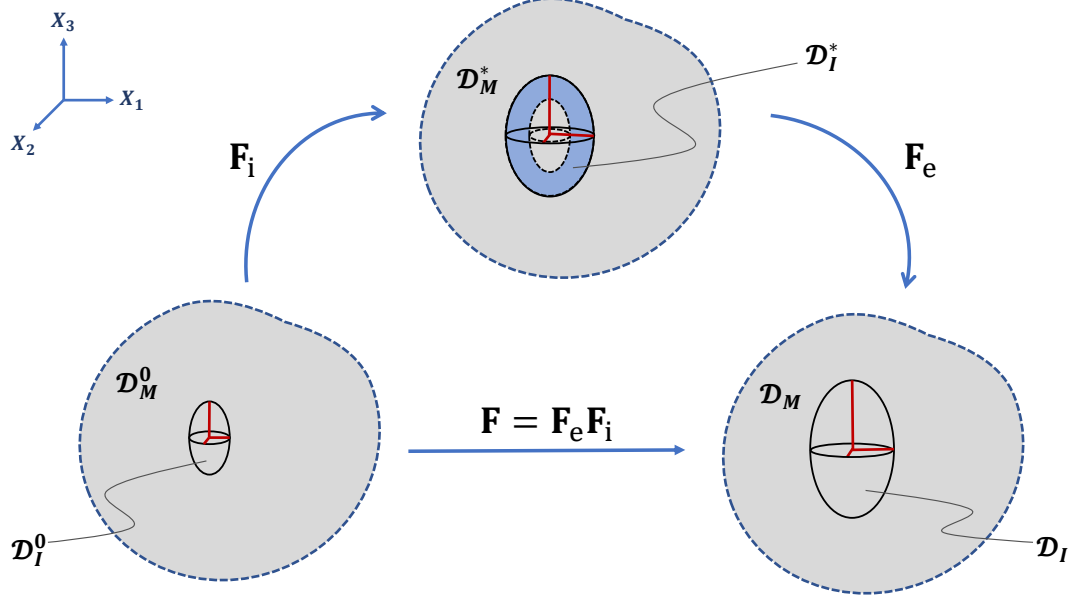


Fig. 9: Schematic illustration of multiplicative decomposition of total deformation gradient \mathbf{F} into elastic \mathbf{F}_e and inelastic (transformation or eigen) \mathbf{F}_i part. The \mathbf{F}_i represents the local stress-free lattice distortion (e.g., due to phase transformation or compositional misfit), while \mathbf{F}_e carries the elastic accommodation required to maintain compatibility and equilibrium.

The elastic part \mathbf{F}_e then maps Ω^* to the current configuration Ω :

$$\mathcal{D}_M = \mathbf{F}_e(\mathcal{D}_M^*), \quad \mathcal{D}_I = \mathbf{F}_e(\mathcal{D}_I^*). \quad (8)$$

For coherent transformations, \mathbf{F}_i is typically phase-wise constant, e.g.

$$\mathbf{F}_i(\mathbf{X}) = \begin{cases} \mathbf{I}, & \mathbf{X} \in \mathcal{D}_M^0, \\ \mathbf{F}_i^{(I)}, & \mathbf{X} \in \mathcal{D}_I^0, \end{cases} \quad (9)$$

while \mathbf{F}_e enforces compatibility and mechanical equilibrium.

3.1 Hyperelastic constitutive models

A hyperelastic constitutive model assumes the existence of a strain-energy density function that ensures thermodynamic consistency [35–38]. Let $W(\mathbf{F}, \mathbf{F}_i)$ denote the strain-energy density per unit reference volume. The stress response is obtained by

differentiating the strain-energy density with respect to the deformation gradient:

$$\mathbf{P}(\mathbf{X}) = \frac{\partial W(\mathbf{F}, \mathbf{F}_i)}{\partial \mathbf{F}}, \quad (10)$$

where $\mathbf{P}(\mathbf{X})$ represents the first Piola-Kirchhoff stress. Table 3 shows two most commonly used hyperelastic constitutive models and their corresponding strain-energy density functions. Both SVK and Hencky assume quadratic forms with a 4th-order elastic stiffness tensor \mathbb{C} . The SVK hyperelastic model assumes a quadratic strain-energy density form in terms of the elastic Green-Lagrange strain tensor (\mathbf{E}_e), whereas the Hencky hyperelastic model describes strain-energy density as a quadratic function of the logarithmic strain tensor (logarithmic elastic Cauchy-Green tensor). Thus, both models are a geometrically nonlinear extension of linear elasticity where they retain the same quadratic nature in the strain measure, but replace small engineering strain with finite strain measures. Moreover, both models recover classical linear elastic material behavior. The SVK hyperelastic law is well-behaved for low-to-moderate strain, however, at large deformation, it may predict nonphysical softening or negative tangent stiffness [39]. The Hencky hyperelastic model overcomes these shortcomings of SVK at large strains since logarithmic strain is additive for successive deformations. However, Hencky hyperelastic model poses increased computational complexity due to the need for spectral decomposition of \mathbf{C}_e to compute $\ln(\mathbf{C}_e)$ and its derivatives [40].

Model	Strain-Energy Density Function	Note
St. Venant–Kirchhoff (SVK) [41, 42]	$W = \frac{1}{2} \mathbf{E}_e : \mathbb{C} : \mathbf{E}_e$	
Hencky (logarithmic) [43]	$W = \frac{1}{2} \varepsilon_H : \mathbb{C}_H : \varepsilon_H$	(SVK is recovered if $\mathbb{C}_H = \mathbb{C}$ and $\log \mathbf{C}_e \approx \mathbf{C}_e - \mathbf{I}$.)

Table 3: Common hyperelastic constitutive models and their strain energy density functions W . $\mathbf{E}_e = \frac{1}{2}(\mathbf{C}_e - \mathbf{I})$, $\mathbf{C}_e = \mathbf{F}_e^T \mathbf{F}_e$

In this work, we employ the St. Venant–Kirchhoff (SVK) hyperelastic model, which leads to stress relation as

$$\mathbf{P} = \frac{\partial W}{\partial \mathbf{F}} = \mathbf{F}_e (\mathbb{C} : \mathbf{E}_e) \mathbf{F}_i^{-T}. \quad (11)$$

3.2 Variational formulation and Hill–Mandel consistency

Let us adopt the additive scale split of the deformation gradient

$$\mathbf{F}(\mathbf{X}) = \bar{\mathbf{F}} + \tilde{\mathbf{F}}(\mathbf{X}) \quad \text{with} \quad \tilde{\mathbf{F}} = \nabla_{\mathbf{X}} \tilde{\mathbf{w}}, \quad \langle \tilde{\mathbf{F}} \rangle = \mathbf{0}, \quad (12)$$

where $\bar{\mathbf{F}}$ is a uniform macroscopic deformation gradient and $\tilde{\mathbf{w}}$ is a periodic displacement fluctuation with zero mean.

Define the macroscopic potential as a function of homogeneous deformation gradient and fluctuating periodic displacement field :

$$\Pi(\bar{\mathbf{F}}, \tilde{\mathbf{w}}) = \int_{V_0} W(\bar{\mathbf{F}} + \nabla_{\mathbf{X}} \tilde{\mathbf{w}}, \mathbf{F}_i) dV_0 - V_0 \mathbf{P}_{\text{app}} : \bar{\mathbf{F}}, \quad (13)$$

where \mathbf{P}_{app} represents the applied stress field. For *deformation control*, $\bar{\mathbf{F}}$ is prescribed and not varied:

$$\Pi(\bar{\mathbf{F}}_{\text{presc}}, \tilde{\mathbf{w}}) = \int_{V_0} W(\bar{\mathbf{F}}_{\text{presc}} + \nabla_X \tilde{\mathbf{w}}) dV_0. \quad (14)$$

Mixed control is handled by a partial Legendre transform: apply the $-\Omega \bar{\mathbf{P}} : \bar{\mathbf{F}}$ term only to the controlled components and keep the remaining components of $\bar{\mathbf{F}}$ fixed.

Stationarity and Euler–Lagrange conditions

Take the first variation of (13) with respect to the independent variables $(\tilde{\mathbf{w}}, \bar{\mathbf{F}})$ and using (12) yields

$$\begin{aligned} \delta \Pi &= \int_{V_0} \mathbf{P} : (\delta \bar{\mathbf{F}} + \nabla_{\mathbf{X}} \delta \tilde{\mathbf{w}}) dV_0 - V_0 \bar{\mathbf{P}} : \delta \bar{\mathbf{F}} \\ &= \int_{V_0} \mathbf{P} : \delta \bar{\mathbf{F}} dV_0 + \int_{V_0} \mathbf{P} : \nabla_{\mathbf{X}} \delta \tilde{\mathbf{w}} dV_0 - V_0 \bar{\mathbf{P}} : \delta \bar{\mathbf{F}} \end{aligned} \quad (15)$$

With $\delta \tilde{\mathbf{w}}$ periodic with zero mean and integrating by parts,

$$\begin{aligned} \int_V \mathbf{P} : \nabla_{\mathbf{X}} \delta \tilde{\mathbf{w}} dV &= - \int_V (\nabla_{\mathbf{X}} \cdot \mathbf{P}) \cdot \delta \tilde{\mathbf{w}} dV_0 + \int_{\partial V_0} (\mathbf{P} \mathbf{n}) \cdot \delta \tilde{\mathbf{w}} dS_0 \\ &= - \int_V (\nabla_{\mathbf{X}} \cdot \mathbf{P}) \cdot \delta \tilde{\mathbf{w}} dV_0, \end{aligned} \quad (16)$$

the term $\int_{\partial V_0} (\mathbf{P} \mathbf{n}) \cdot \delta \tilde{\mathbf{w}} dS_0$ vanishes since opposite periodic faces cancel in the boundary term. Since $\delta \tilde{\mathbf{w}}$ and $\delta \bar{\mathbf{F}}$ are arbitrary,

$$\nabla_{\mathbf{X}} \cdot \mathbf{P}(\mathbf{F}) = \mathbf{0}, \quad (17a)$$

$$\bar{\mathbf{P}}(\mathbf{F}) = \mathbf{P}_{\text{app}}, \quad (17b)$$

where $\bar{\mathbf{P}}(\mathbf{F}) = \frac{1}{V_0} \int_{V_0} \mathbf{P}(\mathbf{F}) dV_0$. Equation (17a) is microequilibrium under periodic kinematics; Equation (17b) is macroequilibrium and embodies Hill–Mandel work consistency and energy equivalency between scales [44, 45]. For traction-free conditions, $\mathbf{P}_{\text{app}} = \mathbf{0}$ and $\bar{\mathbf{F}}$ relaxes such that $\bar{\mathbf{P}} = \mathbf{0}$. This ensures that the macroscopic constitutive response is energetically consistent with the underlying microstructure and provides a variational foundation for homogenization. In many physical systems, the boundary response is neither perfectly clamped nor completely free; certain macroscopic deformation components are prescribed while others are allowed to relax. To represent such intermediate conditions, the stationarity conditions can be generalized

through a mask tensor that selects the controlled deformation and stress components. Readers can refer to supplementary document for detailed derivation of stationarity conditions under mixed boundary conditions.

3.2.1 Hill–Mandel work equivalence

The foundation of computational homogenization rests on thermodynamic law that ensures conservation of energy throughout the transition of scales. Hill–Mandel work equivalency principle states that under (12), periodic admissibility for $\tilde{\mathbf{w}}$, and the stationarity conditions (17a)–(17b), the macroscopic and microscopic virtual work are equal:

$$\langle \mathbf{P} : \delta \mathbf{F} \rangle = \mathbf{P}_{\text{app}} : \delta \bar{\mathbf{F}}. \quad (18)$$

With $\delta \mathbf{F} = \delta \bar{\mathbf{F}} + \nabla_{\mathbf{X}} \delta \tilde{\mathbf{w}}$,

$$\begin{aligned} \langle \mathbf{P} : \delta \mathbf{F} \rangle &= \langle \mathbf{P} \rangle : \delta \bar{\mathbf{F}} + \frac{1}{V_0} \int_{V_0} \mathbf{P} : \nabla_{\mathbf{X}} \delta \tilde{\mathbf{w}} \, dV_0 \\ &= \bar{\mathbf{P}} : \delta \bar{\mathbf{F}} + \frac{1}{V_0} \left[- \int_{V_0} (\nabla_{\mathbf{X}} \cdot \mathbf{P}) \cdot \tilde{\mathbf{w}} \, dV_0 + \int_{\partial V_0} (\mathbf{P} \mathbf{n}) \cdot \tilde{\mathbf{w}} \, dS_0 \right] \\ &= \mathbf{P}_{\text{app}} : \delta \bar{\mathbf{F}}. \end{aligned} \quad (19)$$

The first bracketed term vanishes by (17a), the boundary term cancels by periodicity (opposite faces contribute equal and opposite energy).

If $\bar{\mathbf{F}}$ is prescribed, then $\bar{\mathbf{P}} = \langle \mathbf{P} \rangle$ (resultant) and $\langle \mathbf{P} : \delta \mathbf{F} \rangle = \langle \mathbf{P} \rangle : \delta \bar{\mathbf{F}}$, since the fluctuation work $\langle \mathbf{P} : \nabla \delta \tilde{\mathbf{w}} \rangle$ vanishes by the same argument.

3.2.2 Phase-field model for twin growth

The phase-field order parameter $\Phi_p(\mathbf{X})$ represents the volume fraction of the p^{th} twin variant (out of a total of N_{tw}) at material point \mathbf{X} in the reference configuration. The order parameter exhibits the following values

$$\Phi_p(\mathbf{X}) = \begin{cases} 0 & \forall \mathbf{X} \in \text{parent} \\ (0, 1) & \forall \mathbf{X} \in \text{twin boundary} \\ 1 & \forall \mathbf{X} \in \text{twin} \end{cases} \quad (20)$$

The total Helmholtz free energy of the system is expressed as

$$\Psi = \int_{V_0} \left[\Psi_{\text{bulk}}(\Phi_p, \mathbf{F}, \mathbf{F}_i) + \sum_{p=1}^{N_{\text{tw}}} \mathbf{K}_0^{(p)} : (\nabla_X \Phi_p \otimes \nabla_X \Phi_p) \right] dV_0, \quad (21)$$

where Ψ_{bulk} represents bulk free-energy density, and \mathbf{K}_0^p denotes gradient energy coefficient for p^{th} twin variant measured in reference configuration. The bulk free-energy density is decomposed as

$$\Psi_{\text{bulk}} = W(\mathbf{F}, \mathbf{F}_i) + \Psi_{\text{ch}}(\Phi_p) + \Psi_{\text{int}}(\Phi_p), \quad (22)$$

where $\Psi_{\text{ch}}(\Phi_p) = 2 \sum_{p=1}^{N_t} A_p \Phi_p^2 (1 - \Phi_p)^2$, A_p is the barrier potential coefficient for the p^{th} twin variant and Ψ_{int} penalizes the coexistence of multiple variants. The interaction energy density is taken as

$$\Psi_{\text{int}} = B \sum_{p < q} \Phi_p^2 \Phi_q^2; \quad B > 0,$$

where B represents the strength of repulsive interaction that controls how energetically unfavorable it is for two or more twin variants to coexist at the same spatial point.

The evolution of the non-conserved order parameter $\Phi(\mathbf{X}, t)$ follows the time-dependent Ginzburg–Landau (TDGL) equation:

$$\frac{\partial \Phi_p}{\partial t} = -M(\mathbf{X}) \frac{\delta \Psi}{\delta \Phi_p}, \quad (23)$$

where $M(\mathbf{X})$ is the interface mobility in reference configuration and $\delta \Psi / \delta \Phi_p$ is the variational derivative of the total energy with respect to Φ_p . The TDGL equation (also known as the Allen–Cahn equation) describes relaxational dynamics toward thermodynamic equilibrium for systems with a non-conserved order parameter [6, 46]. Expanding the variational derivative gives

$$\frac{\delta \Psi}{\delta \Phi_p} = \frac{\partial W}{\partial \Phi_p} + \frac{\partial \Psi_{\text{ch}}(\Phi_p)}{\partial \Phi_p} + \frac{\partial \Psi_{\text{int}}(\Phi_p)}{\partial \Phi_p} + 2\kappa_0^{(p)} \nabla_X^2 \Phi_p, \quad (24)$$

where the first term represents the elastic driving force:

$$\frac{\partial W}{\partial \Phi_p} = -\mathbf{F}^T \mathbf{F}_i^{-T} \mathbf{P}_e \mathbf{F}_i^{-T} : \frac{\partial \mathbf{F}_i}{\partial \Phi_p}, \quad \frac{\partial \mathbf{F}_i}{\partial \Phi_p} = h'(\Phi_p) \gamma_p (\mathbf{s}_p \otimes \mathbf{m}_p). \quad (25)$$

Here \mathbf{P}_e is the elastic first Piola–Kirchhoff and obtained as $\mathbf{P}_e = \mathbf{F}_e \mathbf{S}$, and \mathbf{S} denotes second Piola–Kirchhoff stress tensor. The detailed derivation of elastic driving force is represented in C. The transformation deformation gradient is defined as

$$\mathbf{F}_i(\eta_p) = \mathbf{I} + \sum_{p=1}^{N_{\text{tw}}} h(\Phi_p) \gamma_p (\mathbf{s}_p \otimes \mathbf{m}_p), \quad (26)$$

where $h(\Phi_p) = 3\Phi_p^2 - 2\Phi_p^3$ ensures a smooth transition between the untwinned ($\Phi_p = 0$) and fully twinned ($\Phi_p = 1$) states, γ_p is the twinning shear magnitude, and $(\mathbf{s}_p, \mathbf{m}_p)$ specify the shear direction and twin-plane normal of variant p .

The position dependent interface mobility is expressed as

$$M(X) = M_0(1 + a_x n_x^2 + a_y n_y^2 + a_z n_z^2), \quad n_x^2 + n_y^2 + n_z^2 = 1, \quad (27)$$

where M_0 is the constant contribution to the interface mobility ($M_0 > 0$), a_x, a_y, a_z represent weight contributions of respective direction to mobility, and c_x, c_y, c_z represent normalized components of interface normal. The choice of a_x, a_y , and a_z decides

relative contributions to the resultant mobility. When $a_x = a_y = a_z = 0$ then resultant mobility becomes isotropic $M = M_0$.

3.2.3 Thermodynamic and Kinematic Consistency

In the present formulation, the Allen–Cahn equation is solved in the reference configuration where the order parameter $\Phi(\mathbf{X}, t)$ evolves according to relaxation dynamics. The total free energy functional is expressed as

$$\Psi = \int_{V_0} [\psi(\Phi, \mathbf{F}) + \mathbf{K}_0 : (\nabla_X \Phi \otimes \nabla_X \Phi)] dV, \quad (28)$$

where ψ denotes the homogeneous free energy density and \mathbf{K}_0 is the gradient-energy coefficient defined per unit reference volume.

Frame indifference necessitates that Ψ remains invariant under a superposed rigid body motion $\mathbf{F} \rightarrow \mathbf{Q}\mathbf{F}$, with $\mathbf{Q} \in \text{SO}(3)$. In general, interfacial energies and mobilities are determined experimentally in the *current* configuration; therefore, referential quantities must be obtained by an appropriate pull-back operation. For the gradient term, the pull-back of the spatial modulus κ_s is

$$\mathbf{K}_0 = J \mathbf{F}^{-1} \kappa_s \mathbf{F}^{-T}, \quad (29)$$

where $J = \det \mathbf{F}$. If the interface exhibits isotropic interfacial energy such that $\kappa_s = \kappa \mathbf{I}$, Eq. (29) reduces to

$$\mathbf{K}_0 = J \kappa \mathbf{C}^{-1}, \quad \mathbf{C} = \mathbf{F}^T \mathbf{F}, \quad (30)$$

ensuring that the gradient contribution to the free energy is objective.

The evolution of Φ follows the Allen–Cahn kinetics in the reference configuration,

$$\dot{\Phi} = -M \mu_\Phi, \quad \mu_\Phi = \frac{\partial \psi}{\partial \Phi} - \nabla_X (2\mathbf{K}_0 \nabla_X \Phi), \quad (31)$$

where M denotes the referential interface mobility. Since interface mobilities are likewise measured in the spatial configuration, objectivity and thermodynamic consistency require the pull-back transformation

$$M = J M_s, \quad (32)$$

which preserves the dissipation rate $\mathcal{D} = \int_{V_0} L_0 \mu_\Phi^2 dV \geq 0$. This guarantees that the evolution law satisfies the second law of thermodynamics while remaining invariant under superposed rigid motions.

In the small-strain limit ($J \approx 1$, $\mathbf{C}^{-1} \approx \mathbf{I}$), the referential and spatial quantities coincide, and the formulation naturally reduces to the classical Allen–Cahn equation with constant isotropic coefficients.

3.3 Numerical implementation

3.3.1 Mechanical Equilibrium

The stationarity condition (17a) represents the static equilibrium condition at micro scale. Let us rewrite it as a Lippmann–Schwinger-type fixed point using a linear reference stiffness \mathbb{C} . The spatial heterogeneity of stress is given as

$$\mathbf{P}(\mathbf{X}) = \mathbb{C} : \mathbf{F}(\mathbf{X}) + \mathbf{P}(\mathbf{X}) - \mathbb{C} : \mathbf{F}(\mathbf{X}) = \mathbb{C} : \mathbf{F}(\mathbf{X}) + \boldsymbol{\tau}(\mathbf{X}), \quad (33)$$

where $\boldsymbol{\tau}(\mathbf{X})$ represents the polarization stress field. Thus, the stationary condition (17a) modifies as

$$\nabla_{\mathbf{X}} \cdot \mathbf{P} = 0, \quad (34a)$$

$$\nabla_{\mathbf{X}} \cdot (\mathbb{C} : \mathbf{F}(\mathbf{X}) + \boldsymbol{\tau}(\mathbf{X})) = 0, \quad (34b)$$

$$\nabla_{\mathbf{X}} \cdot \{\mathbb{C} : [\nabla_{\mathbf{X}} \otimes \boldsymbol{\chi}(\mathbf{X})] + \boldsymbol{\tau}(\mathbf{X})\} = 0 \quad (34c)$$

Applying Fourier transform to (34c) and simplifying further yields

$$\mathbb{C} : [\boldsymbol{\chi}(\mathbf{k}) \otimes \mathbf{k}] \cdot \mathbf{k} = \boldsymbol{\tau}(\mathbf{k}) \cdot i\mathbf{k}, \quad (35)$$

$$\mathbf{G}(\mathbf{k}) \cdot \boldsymbol{\chi}(\mathbf{k}) = \boldsymbol{\tau}(\mathbf{k}) \cdot i\mathbf{k} \quad \forall \quad \mathbf{k} \neq 0 \quad (36)$$

where \mathbf{k} represents Fourier wave vector and $i = \sqrt{-1}$ and $\mathbf{G}(\mathbf{k}) = \mathbb{C} : (\mathbf{k} \otimes \mathbf{k})$. The deformation can be expressed as

$$\boldsymbol{\chi}(\mathbf{k}) = \begin{cases} \mathbf{G}^{-1}(\mathbf{k}) \cdot \boldsymbol{\tau} \cdot i\mathbf{k} & \forall \mathbf{k} \neq 0 \\ \boldsymbol{\chi}(0) & \forall \mathbf{k} = 0 \end{cases} \quad (37)$$

The deformation gradient field in Fourier space is expressed as

$$\mathbf{F}(\mathbf{k}) = \begin{cases} -\mathbf{G}^{-1}(\mathbf{k}) \cdot \boldsymbol{\tau}(\mathbf{k}) \cdot (\mathbf{k} \otimes \mathbf{k}) \\ \mathbf{F}(0) \end{cases} = \begin{cases} -\boldsymbol{\Gamma}(\mathbf{k}) : \boldsymbol{\tau}(\mathbf{k}) & \forall \mathbf{k} \neq 0 \\ \bar{\mathbf{F}} & \forall \mathbf{k} = 0 \end{cases} \quad (38)$$

where $\boldsymbol{\Gamma}(\mathbf{k}) = \mathbf{G}^{-1}(\mathbf{k})(\mathbf{k} \otimes \mathbf{k})$ represents Gamma operator.

Using spectral fixed-point iteration method as mentioned in [16], the solution to fluctuating deformation gradient at iteration $n + 1$ is obtained as

$$\{\tilde{\mathbf{F}}(\mathbf{X})\}_{n+1} = \{\tilde{\mathbf{F}}(\mathbf{X})\}_n - \mathcal{F}^{-1} \left(\begin{cases} \boldsymbol{\Gamma}(\mathbf{k}) : \{\mathbf{P}(\mathbf{k})\}_n & \forall \mathbf{k} \neq 0, \\ \mathbf{0} & \forall \mathbf{k} = 0, \end{cases} \right) \quad (39)$$

which forms the basis for the updated constitutive response $\{\mathbf{P}(\mathbf{X})\}_{n+1}$ in the next iteration. The convergence of (39) is achieved when $\sqrt{\sum |\hat{\mathbf{P}}(\mathbf{k}) \cdot i\mathbf{k}|^2 / N^2} / \|\hat{\mathbf{P}}(0)\|_2 < \varepsilon_{\text{tol}}^{\text{micro}}$.

The second stationarity condition emerging from the variational potential,

$$\bar{\mathbf{P}}(\mathbf{F}) = \mathbf{P}_{\text{app}},$$

ensures energetic consistency between microscopic and macroscopic fields (Hill–Mandel macrohomogeneity). This relation is enforced by iteratively adjusting the macroscopic deformation gradient $\bar{\mathbf{F}}$ until the residual

$$\mathbf{R} = \bar{\mathbf{P}}(\mathbf{F}) - \mathbf{P}_{\text{app}}$$

vanishes. A first-order Taylor expansion of \mathbf{P} with respect to $\bar{\mathbf{F}}$ provides the linearized update

$$\mathbf{R} \approx \left\langle \frac{d\mathbf{P}}{d\mathbf{F}} \right\rangle : \Delta \bar{\mathbf{F}} = \bar{\mathbb{K}} : \Delta \bar{\mathbf{F}}, \quad (40)$$

where $\bar{\mathbb{K}} = \langle d\mathbf{P}/d\mathbf{F} \rangle$ is the *macroscopic tangent modulus*, obtained by volume-averaging the consistent local tangent $\mathbb{K}(\mathbf{X})$. Solving $\bar{\mathbb{K}} : \Delta \bar{\mathbf{F}} = -\mathbf{R}$ yields the incremental macro-update

$$\bar{\mathbf{F}}^{(k+1)} = \bar{\mathbf{F}}^{(k)} + \alpha \Delta \bar{\mathbf{F}},$$

where the step length $\alpha \in (0, 1]$ is found by backtracking line search to guarantee monotonic reduction of $\|\mathbf{R}\|_{\infty}$. Regularization is introduced through a small positive parameter ρ_{reg} to stabilize near-singular tangent operators, so that the linear system is solved in the form

$$(\bar{\mathbb{K}} + \rho_{\text{reg}}\mathbb{I}) \Delta \bar{\mathbf{F}} = -\mathbf{R}. \quad (41)$$

This macro-update scheme realizes the second stationary condition of the variational principle and enforces the Hill–Mandel energy equivalence between scales. In the limit of convergence ($\mathbf{R} \rightarrow 0$), the macroscopic stress and deformation satisfy $\langle \mathbf{P} \rangle = \mathbf{P}_{\text{app}}$, which defines the homogenized constitutive response of the periodic medium. Closed-form expression for $d\mathbf{P}/d\mathbf{F}$ for SVK hyperelastic model is given in A.

The coupled micro-macro mechanical equilibrium problem is solved through the iterative scheme summarized in Algorithm 1. The algorithm alternates between a microscopic fixed-point iteration enforcing $\nabla_{\mathbf{X}} \cdot \mathbf{P} = 0$ (microequilibrium) and a macroscopic Newton update enforcing the Hill–Mandel condition $\bar{\mathbf{P}} = \mathbf{P}_{\text{app}}$. In the *MicroSolve* step, the periodic fluctuation field $\tilde{\mathbf{F}} = \nabla_{\mathbf{X}} \tilde{\mathbf{w}}$ is updated in Fourier space using the Green operator $\Gamma(\mathbf{k}) = \mathbf{G}^{-1}(\mathbf{k})(\mathbf{k} \otimes \mathbf{k})$ until the local equilibrium residual falls below a specified tolerance $\text{tol}_{\text{micro}}$. The constitutive response is evaluated through the St. Venant–Kirchhoff hyperelastic model, with the multiplicative decomposition $\mathbf{F} = \mathbf{F}_e \mathbf{F}_i$, where \mathbf{F}_i represents a prescribed eigen-deformation field. For stress-controlled loading, the macroscopic deformation gradient $\bar{\mathbf{F}}$ is updated iteratively to drive the residual $\mathbf{R} = \bar{\mathbf{P}} - \mathbf{P}_{\text{app}}$ to zero. The increment $\Delta \bar{\mathbf{F}}$ is obtained from the linearized macroequilibrium equation $(\bar{\mathbb{K}} + \rho_{\text{reg}}\mathbb{I}) \Delta \bar{\mathbf{F}} = -\mathbf{R}$, where $\bar{\mathbb{K}} = \langle d\mathbf{P}/d\mathbf{F} \rangle$ is the homogenized tangent modulus. A backtracking line search with minimum step α_{min} ensures monotonic reduction of the residual norm $\|\mathbf{R}\|_{\infty}$. Upon convergence, the algorithm delivers a self-consistent solution satisfying both local and global mechanical equilibrium, thereby fulfilling the Hill–Mandel energy equivalence.

Algorithm 1 Coupled Micro–Macro Mechanical Equilibrium

Require: Grid Ω ; $\phi(\mathbf{X})$; \mathbf{F}_i ; (C_{11}, C_{12}, C_{44}) ; $\text{BC} \in \{\text{StrainCtrl}, \text{StressCtrl}\}$; tolerances $\varepsilon_{\text{tol}}^{\text{micro}}, \varepsilon_{\text{tol}}^{\text{macro}}$; **set** $\rho_{\text{reg}} = 10^{-3}$, $\alpha_{\text{min}} = 0.03125$

- 1: Initialize $\tilde{\mathbf{F}} \leftarrow \mathbf{0}$, $\bar{\mathbf{F}} \leftarrow \mathbf{I}$ (or \mathbf{F}_{app}); build $\mathbf{G}^{-1}(\hat{\mathbf{n}})$ for all $\mathbf{k} \neq 0$
- 2: **function** $\text{MICROSOLVE}(\bar{\mathbf{F}}, \tilde{\mathbf{F}})$ ▷ Equation (17a)
- 3: **repeat**
- 4: $\mathbf{F} \leftarrow \bar{\mathbf{F}} + \tilde{\mathbf{F}}$; $\mathbf{F}_e \leftarrow \mathbf{F}\mathbf{F}_i^{-1}$; $\mathbf{C}_e \leftarrow \mathbf{F}_e^T \mathbf{F}_e$
- 5: **StVK:** $\mathbf{S} \leftarrow \mathbb{C} : \frac{1}{2}(\mathbf{C}_e - \mathbf{I})$; **Hencky:** $\mathbf{S} \leftarrow \mathbb{C} : \frac{1}{2} \log \mathbf{C}_e$
- 6: $\mathbf{P} \leftarrow \mathbf{F}_e \mathbf{S} \mathbf{F}_i^{-T}$; $\hat{\mathbf{P}} \leftarrow \mathcal{F}[\mathbf{P}]$
- 7: $\widehat{\Delta \mathbf{F}}(\mathbf{k}) \leftarrow -(\mathbf{G}^{-1} \hat{\mathbf{P}}) \hat{\mathbf{n}} \otimes \hat{\mathbf{n}}$ for $\mathbf{k} \neq 0$; else 0
- 8: $\Delta \mathbf{F} \leftarrow \mathcal{F}^{-1}[\widehat{\Delta \mathbf{F}}]$; $\tilde{\mathbf{F}} \leftarrow \tilde{\mathbf{F}} + \Delta \mathbf{F}$
- 9: **until** $\sqrt{\sum |\hat{\mathbf{P}}(\mathbf{k}) \cdot i\mathbf{k}|^2 / N^2} / \|\hat{\mathbf{P}}(0)\|_2 \leq \varepsilon_{\text{tol}}^{\text{micro}}$
- 10: **return** $(\bar{\mathbf{F}}, \tilde{\mathbf{F}})$
- 11: **end function**
- 12: **if** $\text{BC} = \text{StrainControl}$ **then**
- 13: $\text{MICROSOLVE}(\bar{\mathbf{F}}, \tilde{\mathbf{F}})$; **return**
- 14: **else** ▷ Stress control (Hill–Mandel) Equation (17b)
- 15: **for** $it = 1 : \text{maxiter}_{\text{macro}}$ **do**
- 16: $\text{MICROSOLVE}(\bar{\mathbf{F}}, \tilde{\mathbf{F}})$; $\mathbf{R} \leftarrow \bar{\mathbf{P}} - \mathbf{P}_{\text{app}}(\bar{\mathbf{F}})$
- 17: **if** $\|\mathbf{R}\|_{\infty} \leq \varepsilon_{\text{tol}}^{\text{macro}}$ **then return**
- 18: **end if**
- 19: Assemble $\bar{\mathbb{K}} = \langle d\mathbf{P}/d\mathbf{F} \rangle$
- 20: Solve $(\bar{\mathbb{K}} + \rho_{\text{reg}} \mathbb{I}) \Delta \bar{\mathbf{F}} = -\mathbf{R}$; set $\alpha \leftarrow 1$
- 21: **repeat**
- 22: $\bar{\mathbf{F}}_{\text{trial}} \leftarrow \bar{\mathbf{F}} + \alpha \Delta \bar{\mathbf{F}}$; $\text{MICROSOLVE}(\bar{\mathbf{F}}_{\text{trial}}, \tilde{\mathbf{F}})$
- 23: **if** $\|\bar{\mathbf{P}} - \mathbf{P}_{\text{app}}^{(1)}\|_{\infty}$ decreases **then** $\bar{\mathbf{F}} \leftarrow \bar{\mathbf{F}}_{\text{trial}}$; **break**
- 24: **else** $\alpha \leftarrow \alpha/2$
- 25: **end if**
- 26: **until** $\alpha \leq \alpha_{\text{min}}$
- 27: **end for**
- 28: **end if**
- 29: **end if**

3.4 Solution to TDGL equation

In order to obtain semi-implicit solution, the TDGL equation is modified as:

$$\frac{\partial \Phi_p}{\partial t} = -M(\mathbf{X})H(\mathbf{X}) + 2(M(\mathbf{X}) - M_0)\kappa_0^{(p)}\nabla_{\mathbf{X}}^2\Phi_p + 2M_0\kappa_0^{(p)}\nabla_{\mathbf{X}}^2\Phi_p, \quad (42)$$

where $H(\mathbf{X}) = \frac{\partial W}{\partial \Phi_p} + \frac{\partial \Psi_{\text{ch}}(\Phi_p)}{\partial \Phi_p} + \frac{\partial \Psi_{\text{int}}(\Phi_p)}{\partial \Phi_p}$. Let $R(\mathbf{X}) = -M(\mathbf{X})H(\mathbf{X}) + 2(M(\mathbf{X}) - M_0)\kappa_0^{(p)}\nabla_{\mathbf{X}}^2\Phi_p$. Treating nonlinear term $R(\mathbf{X})$ explicit and linear term implicit, the

temporal update to the order parameter reads as:

$$\widehat{\Phi}_p(\boldsymbol{\kappa}, t + \Delta t) = \frac{\widehat{\Phi}_p(\boldsymbol{\kappa}, t) + \Delta t \widehat{R}(\boldsymbol{\kappa})}{1 + \Delta t M_0 \kappa |k|^2} \quad (43)$$

3.5 Comparison with existing finite-strain microelasticity approaches

Recent work has extended phase-field microelasticity into the finite-strain regime using a variety of spectral and variational ideas. These developments differ primarily in how macroscopic loading is imposed, how admissible variations are defined, and how the micro–macro coupling is enforced. Below, we contrast two representative approaches—Zhao et al. [18] and Shchyglo et al. [47]—with the present variational formulation.

(i) Zhao et al. [18]

Zhao et al. proposed a spectral finite-strain microelasticity framework based on a multiplicative decomposition of the deformation gradient. Their formulation treats the macroscopic deformation gradient as fixed, even when macroscopic stress conditions are applied. As a consequence, the macroscopic field does not evolve in response to externally prescribed stresses. This choice leads to a solution that satisfies $\text{Div } \mathbf{P} = \mathbf{0}$ but does not, in general, satisfy the stationarity conditions associated with variations of the macroscopic deformation gradient. Accordingly, the Hill–Mandel macrohomogeneity condition is not enforced explicitly, and the correspondence between microscopic power expenditure and macroscopic work input remains indirect.

(ii) Shchyglo et al. [47]

Shchyglo et al. introduced an efficient spectral algorithm in which the average deformation gradient is updated through a residual-stress correction step. This update is motivated by linearized arguments and provides a practical mechanism for reducing residual stresses during the iterative solution. While this leads to excellent numerical performance, the correction step is not derived from the Euler–Lagrange equations of a finite-strain energy functional. Therefore, the macrolevel update does not correspond to the stationarity condition associated with variations of the macroscopic deformation gradient, and the Hill–Mandel condition is not enforced in a formally variational sense.

(iii) Present work

The present formulation derives both the microscopic equilibrium equations and the macroscopic loading conditions from the first variation of the total finite-strain free-energy functional. This yields a coupled problem in which:

1. the local mechanical equilibrium $\text{Div } \mathbf{P} = \mathbf{0}$ follows naturally from admissible variations of the deformation map,

2. the macroscopic deformation gradient evolves consistently under either prescribed strain or prescribed stress conditions,
3. the Hill–Mandel macrohomogeneity condition is satisfied by construction, ensuring consistency between microscopic power expenditure and macroscopic work input, and
4. the micro–macro coupling is entirely determined by the variational structure, without requiring heuristic updates or linearized corrections.

As a result, the formulation provides a thermodynamically consistent route for combining finite-strain elasticity, microstructural evolution, and macroscopic loading within a unified spectral framework.

4 Conclusion

A variationally consistent finite-strain microelasticity framework is presented that rigorously couples heterogeneous deformation, eigenstrains, and macroscopic loading. By enforcing mechanical equilibrium through the exact stationarity of the total free energy, the formulation naturally satisfies the Hill–Mandel condition and cleanly separates stress-controlled and strain-controlled boundary conditions without heuristic updates. Using the framework, the phase-field simulations of single twin variant evolution in Magnesium is performed. The framework captures experimentally observed faster lateral growth of twin under deformation- and stress-controlled conditions. However, under the deformation-controlled conditions twin growth is faster than that under the stress-controlled conditions. The faster lateral growth of twin can be attributed to a higher strain energy density and shear stress at the twin interface along the lateral direction.

Beyond these conclusions, the present framework also points toward broader opportunities for refinement and future extension. The framework developed here opens several avenues for advancing large-deformation phase-field simulations. A natural next step is to extend the present formulation to more complex hyperelastic models and to microstructures where mechanical and chemical driving forces evolve on comparable timescales. The approach also provides a foundation for rigorous coupling with crystal plasticity and damage models, enabling the study of microstructure evolution under cyclic, shock, or creep loading conditions where finite-strain effects are essential. The current numerical implementation can also be further improved by exploring adaptive preconditioning, mixed real–Fourier iteration strategies, and more robust linearization schemes to enhance convergence under highly nonlinear conditions. In summary, these developments unlock potential strategies for predictive modelling of material behavior, paving the way toward a unified, thermodynamically consistent, and computationally efficient framework for microstructure–mechanics interactions at finite strain.

Supplementary information.

Acknowledgements. Author acknowledges discussions with Philip Eisenlohr, Michigan State University, USA and Franz Roters, Max-Planck Institute for Sustainable Materials, Germany for their useful comments that have shaped this work in good direction.

Declarations

The code of spectral-Newton update for micro-macro equilibrium will be shared on reasonable requests.

Appendix A Tangent operators for the macro step

We list $\mathbb{K} = d\mathbf{P}/d\mathbf{F}$ as a fourth-order map acting on a perturbation $\delta\mathbf{F}$.

With $\mathbf{F}_e = \mathbf{F}\mathbf{F}_i^{-1}$, $\mathbf{C}_e = \mathbf{F}_e^T \mathbf{F}_e$, $\mathbf{E}_e = \frac{1}{2}(\mathbf{C}_e - \mathbf{I})$, and $\mathbf{S}_e = \mathbb{C} : \mathbf{E}_e$,

$$\mathbb{K}[\delta\mathbf{F}] = \mathbf{F}_e (\mathbb{C} : \frac{1}{2}(\mathbf{F}_e^T \delta\mathbf{F}_e + \delta\mathbf{F}_e^T \mathbf{F}_e) \mathbf{F}_i^{-T} + \delta\mathbf{F}_e \mathbf{S}_e \mathbf{F}_i^{-T}), \quad \delta\mathbf{F}_e = \delta\mathbf{F} \mathbf{F}_i^{-1}. \quad (\text{A1})$$

Appendix B Derivation of 1st Piola–Kirchhoff Stress

St. Venant–Kirchhoff hyperelastic law:

$$W(\mathbf{E}_e) = \frac{1}{2} \mathbf{E}_e : \mathbb{C} : \mathbf{E}_e, \quad \mathbf{E}_e = \frac{1}{2} (\mathbf{C}_e - \mathbf{I}), \quad \mathbf{C}_e = \mathbf{F}_e^T \mathbf{F}_e$$

1st Piola–Kirchhoff stress definition:

$$\mathbf{P} = \frac{\partial W}{\partial \mathbf{F}}$$

2nd Elastic Piola–Kirchhoff stress definition:

$$\mathbf{S}_e = \frac{\partial W}{\partial \mathbf{E}_e} = \mathbb{C} : \mathbf{E}_e$$

Variation of energy:

$$\delta W = \mathbf{S}_e : \delta \mathbf{E}_e$$

With $\delta \mathbf{E}_e = \frac{1}{2} \delta \mathbf{C}_e$ and $\delta \mathbf{C}_e = \mathbf{F}_e^T \delta \mathbf{F}_e + \delta \mathbf{F}_e^T \mathbf{F}_e$,

$$\delta \mathbf{E}_e = \text{sym}(\mathbf{F}_e^T \delta \mathbf{F}_e)$$

Use symmetry of \mathbf{S}_e :

$$\delta W = \mathbf{S}_e : \text{sym}(\mathbf{F}_e^T \delta \mathbf{F}_e) = \mathbf{S}_e : (\mathbf{F}_e^T \delta \mathbf{F}_e) = (\mathbf{F}_e \mathbf{S}_e) : \delta \mathbf{F}_e \quad (\text{B2})$$

From $\mathbf{F} = \mathbf{F}_e \mathbf{F}_i \implies \mathbf{F}_e = \mathbf{F} \mathbf{F}_i^{-1}$, further yields:

$$\delta \mathbf{F}_e = \delta \mathbf{F} \mathbf{F}_i^{-1} \quad (\delta \mathbf{F}_i = 0) \quad (\text{B3})$$

From eqns. (B2) and (B3),

$$\delta W = (\mathbf{F}_e \mathbf{S}_e \mathbf{F}_i^{-T}) : \delta \mathbf{F}$$

Final form of \mathbf{P} :

$$\begin{aligned} \mathbf{P} &= \mathbf{F}_e \mathbf{S}_e \mathbf{F}_i^{-T} \\ \mathbf{P} &= \mathbf{F}_e [\mathbb{C} : \mathbf{E}_e] \mathbf{F}_i^{-T} \end{aligned}$$

Appendix C Elastic driving force

The elastic driving force can be decomposed using chain rule as

$$\frac{\partial W_{\text{el}}}{\partial \Phi} = \frac{\partial W_{\text{el}}}{\partial \mathbf{F}_i} : \frac{\partial \mathbf{F}_i}{\partial \Phi}. \quad (\text{C4})$$

Using multiplicative decomposition of deformation gradient, elastic deformation gradient is given as

$$\mathbf{F}_e = \mathbf{F} \mathbf{F}_i^{-1}$$

Assuming \mathbf{F} is fixed, the variation of elastic deformation gradient yields

$$\delta \mathbf{F}_e = \mathbf{F} (\delta \mathbf{F}_i^{-1}) \quad (\text{C5})$$

To obtain $\delta \mathbf{F}_i^{-1}$, consider the identity:

$$\mathbf{F}_i \mathbf{F}_i^{-1} = \mathbf{I}$$

and take variation

$$\delta(\mathbf{F}_i \mathbf{F}_i^{-1}) = \delta \mathbf{I} = 0.$$

Rearranging terms yields

$$\delta(\mathbf{F}_i^{-1}) = -\mathbf{F}_i^{-1} (\delta \mathbf{F}_i) \mathbf{F}_i^{-1}. \quad (\text{C6})$$

Combining eqns. (C5) and (C6),

$$\delta \mathbf{F}_e = -\mathbf{F} \mathbf{F}_i^{-1} (\delta \mathbf{F}_i) \mathbf{F}_i^{-1} \quad (\text{C7})$$

The variation of W_{el} gives

$$\delta W_{\text{el}} = \mathbf{S} : \delta \mathbf{E}_e,$$

where $\mathbf{S} = \mathbb{C} : \mathbf{E}_e$. The variation of \mathbf{E}_e gives

$$\delta \mathbf{E}_e = \frac{1}{2} \left[(\delta \mathbf{F}_e)^T \mathbf{F}_e + \mathbf{F}_e^T \delta \mathbf{F}_e \right] = \text{sym} (\mathbf{F}_e^T \delta \mathbf{F}_e) \quad (\text{C8})$$

Since \mathbf{S} is symmetric in nature,

$$\delta W_{\text{el}} = \mathbf{S} : \mathbf{F}_e^T \delta \mathbf{F}_e \quad (\text{C9})$$

$$= \mathbf{F}_e \mathbf{S} : \delta \mathbf{F}_e \quad (\text{C10})$$

From eqn. (C7)

$$\delta W_{\text{el}} = \mathbf{P}_e : [-\mathbf{F} \mathbf{F}_i^{-1} (\delta \mathbf{F}_i) \mathbf{F}_i^{-1}] , \quad (\text{C11})$$

where $\mathbf{P}_e = \mathbf{F}_e \mathbf{S}$. Using $\mathbf{A} : (\mathbf{L} \mathbf{X} \mathbf{N}) = (\mathbf{L}^T \mathbf{A} \mathbf{N}^T) : \mathbf{X}$,

$$\delta W_{\text{el}} = -\mathbf{F}^T \mathbf{F}_i^{-T} \mathbf{P}_e \mathbf{F}_i^{-T} : \delta \mathbf{F}_i \quad (\text{C12})$$

Thus,

$$\frac{\partial W_{\text{el}}}{\partial \mathbf{F}_i} = -\mathbf{F}^T \mathbf{F}_i^{-T} \mathbf{P}_e \mathbf{F}_i^{-T} ,$$

and elastic driving force is expressed as

$$\frac{\partial W_{\text{el}}}{\partial \Phi} = -\mathbf{F}^T \mathbf{F}_i^{-T} \mathbf{P}_e \mathbf{F}_i^{-T} : \frac{\partial \mathbf{F}_i}{\partial \Phi} \quad (\text{C13})$$

References

- [1] Porter, D.A., Easterling, K.E.: Phase Transformations in Metals and Alloys. CRC press, Boca Raton (2009)
- [2] Christian, J.: The Theory of Transformations in Metals and Alloys. Permagon, Amsterdam (2002)
- [3] Nishiyama, Z.: Martensitic Transformation, 2nd edn. Elsevier, Amsterdam (2012)
- [4] Khachaturyan, A.G., Morris, G.W.: Theoretical analysis of coherent phase transformations. *Acta Metallurgica* **21**, 147–155 (1973)
- [5] Khachaturyan, A.G., Laughlin, R.S.: Elastic energy of coherently misfitting precipitates. *Acta Metallurgica* **23**, 1113–1123 (1975)
- [6] Khachaturyan, A.G.: Theory of Structural Transformations in Solids. Dover Publication, New York (2013). Reprint of the John Wiley & Sons, 1983
- [7] Levitas, V.I., Levin, V.A., Zingerman, K.M., Freiman, E.I.: Displacive phase transitions at large strains: phase-field theory and simulations. *Physical Review Letters* **103**(2), 025702 (2009)
- [8] Hildebrand, F., Miehe, C.: A phase field model for the formation and evolution of martensitic laminate microstructure at finite strains. *Philosophical Magazine* **92**(34), 4250–4290 (2012)
- [9] Liu, C., Shanthraj, P., Diehl, M., Roters, F., Dong, S., Dong, J., Ding, W., Raabe, D.: An integrated crystal plasticity–phase field model for spatially resolved twin nucleation, propagation, and growth in hexagonal materials. *International Journal of Plasticity* **106**, 203–227 (2018)

- [10] Liu, G., Mo, H., Wang, J., Shen, Y.: Coupled crystal plasticity finite element-phase field model with kinetics-controlled twinning mechanism for hexagonal metals. *Acta Materialia* **202**, 399–416 (2021)
- [11] Rezaee-Hajidehi, M., Sadowski, P., Stupkiewicz, S.: Deformation twinning as a displacive transformation: Finite-strain phase-field model of coupled twinning and crystal plasticity. *Journal of the Mechanics and Physics of Solids* **163**, 104855 (2022)
- [12] Liu, C., Roters, F., Raabe, D.: Finite strain crystal plasticity-phase field modeling of twin, dislocation, and grain boundary interaction in hexagonal materials. *Acta Materialia* **242**, 118444 (2023)
- [13] Finel, A., Le Bouar, Y., Gaubert, A., Salman, U.: Phase field methods: microstructures, mechanical properties and complexity. *Comptes Rendus Physique* **11**(3-4), 245–256 (2010)
- [14] Vattré, A., Denoual, C.: Polymorphism of iron at high pressure: a 3d phase-field model for displacive transitions with finite elastoplastic deformations. *Journal of the Mechanics and Physics of Solids* **92**, 1–27 (2016)
- [15] Levitas, V.I.: Phase field approach to martensitic phase transformations with large strains and interface stresses. *Journal of the Mechanics and Physics of Solids* **70**, 154–189 (2014)
- [16] Eisenlohr, P., Diehl, M., Lebensohn, R.A., Roters, F.: A spectral method solution to crystal elasto-viscoplasticity at finite strains. *International Journal of Plasticity* **46**, 37–53 (2013)
- [17] Borukhovich, E., Engels, P., Böhlke, T., Shchyglo, O., Steinbach, I.: Large strain elasto-plasticity for diffuse interface models. *Modelling and Simulation in Materials Science and Engineering* **22**(3), 034008 (2014)
- [18] Zhao, P., Low, T.S.E., Wang, Y., Niezgoda, S.R.: Finite strain phase-field microelasticity theory for modeling microstructural evolution. *Acta Materialia* **191**, 253–269 (2020)
- [19] Eshelby, J.D.: The determination of the elastic field of an ellipsoidal inclusion, and related problems. *Proceedings of the royal society of London. Series A. Mathematical and physical sciences* **241**(1226), 376–396 (1957)
- [20] Eshelby, J.D.: The elastic field outside an ellipsoidal inclusion. *Proceedings of the royal society of London. Series A. Mathematical and physical sciences* **252**(1271), 561–569 (1959)
- [21] Barber, J.R.: *Elasticity*, 4th edn. Springer, Cham (2004)

- [22] Christian, J.W., Mahajan, S.: Deformation twinning. *Progress in materials science* **39**(1-2), 1–157 (1995)
- [23] Wang, J., Yadav, S., Hirth, J., Tomé, C., Beyerlein, I.: Pure-shuffle nucleation of deformation twins in hexagonal-close-packed metals. *Materials Research Letters* **1**(3), 126–132 (2013)
- [24] Orozco-Caballero, A., Lunt, D., Robson, J.D., Da Fonseca, J.Q.: How magnesium accommodates local deformation incompatibility: a high-resolution digital image correlation study. *Acta Materialia* **133**, 367–379 (2017)
- [25] Hu, S., Henager Jr, C.H., Chen, L.: Simulations of stress-induced twinning and de-twinning: a phase field model. *Acta Materialia* **58**(19), 6554–6564 (2010)
- [26] Heo, T.W., Wang, Y., Bhattacharya, S., Sun, X., Hu, S., Chen, L.-Q.: A phase-field model for deformation twinning. *Philosophical Magazine Letters* **91**(2), 110–121 (2011)
- [27] Kondo, R., Tadano, Y., Shizawa, K.: A phase-field model of twinning and detwinning coupled with dislocation-based crystal plasticity for hcp metals. *Computational materials science* **95**, 672–683 (2014)
- [28] Liu, H., Lin, F., Zhao, P., Moelans, N., Wang, Y., Nie, J.: Formation and autocatalytic nucleation of co-zone $\{10\bar{1}2\}$ deformation twins in polycrystalline Mg: A phase field simulation study. *Acta Materialia* **153**, 86–107 (2018)
- [29] Liu, Y., Tang, P., Gong, M., McCabe, R., Wang, J., Tomé, C.: Three-dimensional character of the deformation twin in magnesium. *Nature communications* **10**(1), 3308 (2019)
- [30] Lee, S., Pilipchuk, M., Yildirim, C., Greeley, D., Shi, Q., Berman, T.D., Creuziger, A., Rust, E., Detlefs, C., Sundararaghavan, V., *et al.*: Three-dimensional nucleation and growth of deformation twins in magnesium. *Science* **389**(6760), 632–636 (2025)
- [31] Wang, Y., Chen, L.-Q., Liu, Z.-K., Mathaudhu, S.: First-principles calculations of twin-boundary and stacking-fault energies in magnesium. *Scripta Materialia* **62**(9), 646–649 (2010)
- [32] Kim, S.G., Kim, W.T., Suzuki, T.: Phase-field model for binary alloys. *Physical review e* **60**(6), 7186 (1999)
- [33] Long, T., Smith, C.S.: Single-crystal elastic constants of magnesium and magnesium alloys. *Acta Metallurgica* **5**(4), 200–207 (1957)
- [34] Hosford, W.F.: *Mechanical Behavior of Materials*, 2nd edn. Cambridge university press, New York (2010)

- [35] Simo, J.C., Hughes, T.J.R.: Computational Inelasticity. Interdisciplinary Applied Mathematics, vol. 7. Springer, New York (1998)
- [36] Holzapfel, G.A.: Nonlinear Solid Mechanics: A Continuum Approach for Engineering. John Wiley & Sons, Chichester (2000)
- [37] Truesdell, C., Noll, W.: The non-linear field theories of mechanics. In: Flügge, S. (ed.) Handbuch der Physik, Vol. III/3. Springer, Berlin, Heidelberg (1965). Foundational treatment defining elastic and hyperelastic materials via energy potentials.
- [38] Ogden, R.W.: Non-Linear Elastic Deformations. Dover Publications, New York (1997). Originally published 1984; chapters 2–3 derive stress from strain-energy functions.
- [39] Sautter, K.B., Meßmer, M., Teschemacher, T., Bletzinger, K.-U.: Limitations of the st. venant–kirchhoff material model in large strain regimes. International Journal of Non-Linear Mechanics **147**, 104207 (2022)
- [40] Xiao, H., Bruhns, O.T., Meyers, A.: Logarithmic strain, logarithmic spin and logarithmic rate. Acta Mechanica **124**, 89–105 (1997)
- [41] Kirchhoff, G.: Über das gleichgewicht und die bewegung eines unendlich dünnen elastischen stabes. Journal für die reine und angewandte Mathematik **56**, 285–313 (1859)
- [42] Saint-Venant, A.-J.-C.B.d.: Mémoire sur la torsion des prismes, avec des considérations sur leur flexion, ainsi que sur l’équilibre intérieur des solides élastiques en général, et des formules qui s’y rapportent. Mémoires présentés par divers savants étrangers à l’Académie des Sciences **14**, 233–560 (1855)
- [43] Hencky, H.: The law of elasticity for isotropic and quasi-isotropic substances by finite deformations. Journal of Rheology **2**, 169–176 (1928)
- [44] Hill, R.: Elastic properties of reinforced solids: some theoretical principles. Journal of the Mechanics and Physics of Solids **11**(5), 357–372 (1963)
- [45] Mandel, J.: Plasticité classique et viscoplasticité. In: CISM Courses and Lectures vol. 97. Springer, Vienna (1972)
- [46] Wang, Y., Khachaturyan, A.: Three-dimensional field model and computer modeling of martensitic transformations. Acta materialia **45**(2), 759–773 (1997)
- [47] Shchyglo, O., Ali, M.A., Salama, H.: Efficient finite strain elasticity solver for phase-field simulations. NPJ Computational Materials **10**(1), 52 (2024)